minerals

MDPI

Article

The Geochemical Characteristics and Environmental Implications of the Paleocene–Eocene in the Jiangling Depression, Southwestern Jianghan Basin

Kai Yan [1,2], Chunlian Wang [1,*], Renyi Chen [1], Jiuyi Wang [1], Ruiqin Li [3,4] and Lihong Liu [3,5]

[1] MNR Key Laboratory of Metallogeny and Mineral Assessment, Institute of Mineral Resources, Chinese Academy of Geological Sciences, Beijing 100037, China; yankai_ytq@163.com (K.Y.); cgschenry@126.com (R.C.); wjyhlx@163.com (J.W.)
[2] Institute of Earth Sciences, University of Iceland, Sturlugata 7, 102 Reykjavík, Iceland
[3] School of Earth and Space Sciences, Peking University, Beijing 100871, China; 1601110551@pku.edu.cn (R.L.); liulihong713@163.com (L.L.)
[4] Department of Geological Sciences and Environmental Studies, State University of New York at Binghamton, New York, NY 13902, USA
[5] Oil & Gas Survey, China Geological Survey, Beijing 100083, China
* Correspondence: wangchunlian312@163.com

Abstract: Various isotopic and palynological indicators have shown interspersed periods of aridity and humidity for the late Paleocene to early Eocene in central China, so the paleoclimate conditions remain unclear. This research investigates the environmental characteristics of a saline lake in the Jiangling depression, southwestern Jianghan Basin, from the Paleocene to the Eocene, using bulk-rock geochemistry in a 1280 m sediment core. The ratios of FeO/MnO, Al_2O_3/MgO, and C-value indicate a semi-humid to semi-arid climate in the early–middle Paleocene. There was a rapid shift to a humid climate during the late Paleocene to early Eocene, following a short time of intense dryness. The Eocene climate was arid, but experienced intermittent humidity. The variation trend of the CIA, CIW and PIA was similar to that of FeO/MnO, Al_2O_3/MgO, and the C-value, so chemical weathering of the surrounding rocks was controlled by climate change. The lake redox conditions in the Jiangling depression from the Paleocene to the Eocene were reconstructed using the ratios of U/Th, Ni/Co, and V/Cr. During humidity and alternations of aridity and humidity, the lake water received external water input, resulting in weak stratification, so the sediments were in oxidizing conditions. During aridity, lakes become endorheic, leading to sediments forming in reduced conditions. The salinity of the lake in the Jiangling depression from the Paleocene to the Eocene was determined through analysis of sedimentary sequences and the trend of the Sr/Ba ratio. In the early–middle Paleocene, lake salinity varied greatly. From the late Paleocene to the early Eocene, lake salinity decreased. In the Eocene, lake salinity increased and halite precipitated, but lake salinity finally decreased due to a humid climate. During the late Paleocene–early Eocene, the occurrence of multiple humid climates in the Jiangling depression were not merely regional effects. The most significant humidity was caused by a global hyperthermal (PETM), which caused a huge increase in precipitation in the whole of East Asia and even in low latitudes around the world.

Keywords: Jiangling depression; Paleocene–Eocene saline lake; climate; redox conditions; salinity

Citation: Yan, K.; Wang, C.; Chen, R.; Wang, J.; Li, R.; Liu, L. The Geochemical Characteristics and Environmental Implications of the Paleocene–Eocene in the Jiangling Depression, Southwestern Jianghan Basin. *Minerals* **2024**, *14*, 234. https://doi.org/10.3390/min14030234

Received: 4 November 2023
Revised: 14 February 2024
Accepted: 23 February 2024
Published: 26 February 2024

1. Introduction

The Jianghan Basin is a Mesozoic–Cenozoic rift basin in central China which has experienced multistage tectonic movement. In the Paleocene, the Jianghan Basin deposited abundant evaporites, and potassium and lithium-rich brine ore [1–5]. In view of the sedimentary characteristics of evaporite in a series of rifted basins in south China, Liu et al. (2013, 2016) [3,6] proposed that the formation of evaporite deposits was controlled by

tectonics, provenance, and climate. This is because some scholars once believed that the Jianghan Basin was affected by subtropical highs controlled by the planetary wind system during the late Cretaceous–early Paleogene, and that the climate was mainly hot and arid [7,8]. However, in the early Paleogene (about 59–50 Ma), Earth's surface experienced a series of abrupt, short-term global warming events (called hyperthermals), most notably the Paleocene–Eocene thermal maximum (PETM). The PETM lasted less than 200 kyr, but it resulted in a global temperature increase of about 5–8 °C [9,10], accompanied by a negative carbon isotope excursion (CIE) of 2–7‰ [1–15]. There is evidence that the PETM led to a significant increase in precipitation at the low and middle latitudes of East Asia [16–18]. The latest research results challenge the view that East Asia was in a hot and arid climate for a long time in the early Paleogene. More detailed studies are needed to determine the paleoenvironment and paleoclimate at that time.

At present, there is much research on the climate and environmental characteristics of the early Paleogene in the Jiangling depression, but there are great differences due to the experimental objects and methods. The analysis of palynological types showed that the climate in the Jianghan Basin was subtropical arid during the Paleocene, and alternating between humid and arid in the Eocene [7]. Wang et al. (2013) [1] revealed the change of paleoclimate conditions from hot and arid Paleocene to humid Eocene in the Jiangling depression by using changes in the carbon and oxygen isotope composition of carbonate in lacustrine sediments. Li et al. (2015, 2016) [19,20], based on the fluid inclusion temperature test of anhydrite and halite, believed that the temperature in the early Eocene was between 14.9 and 38.5 °C, a decrease compared with the Paleocene, but the climate was still mainly hot and arid. However, there is evidence that precipitation in the Jianghan Basin increased significantly during the PETM [16,17]. Therefore, we try to use different analysis and testing methods to study the Paleocene–Eocene climate and environmental characteristics of the Jiangling depression, and reveal the influence of the PETM on the hydrological cycles in East Asia.

After many years of development, geochemical parameters have been widely used in paleoenvironmental conditions, tectonic settings, and clastic rock provenance [21–25]. The geochemical indicators of major and trace elements are rarely affected by lithology changes, and are widely used to indicate characteristics of the paleoclimate and paleo-environment from marine and terrestrial sediments [26–30]. Therefore, geochemical data analysis can provide a reliable basis for reconstructing the paleoenvironment of evaporite sedimentary strata in the Jiangling depression.

2. Geological Setting

The Jianghan Basin located in the Yangtze Block of central China, is a large Mesozoic–Cenozoic rift basin, with a total area of 36,360 km^2 [31–33]. It is surrounded by various geological features, such as the Qinling orogen in the north, the Dabie Terrance in the northeast, the Edong fold–thrust belt in the east, the Jiangnan orogen in the south, and the Huangling massif and Xiang'exi fold-thrust belt in the west [34–38] (Figure 1A). The Presinian metamorphic basement of the Jianghan Basin was formed during the late Proterozoic. The basement of the Jianghan Basin consists of two parts: the underlying crystalline basement and the overlying pre-rift strata. The crystalline basement of the Jianghan Basin mainly consists of Archean–Proterozoic metamorphic and metasedimentary rocks [37]. During the Sinian to the early Triassic, with the influence of the regional Indosinian movement spreading to this area, the Jianghan Basin uplifted to various degrees against a background of dramatic and rapid crustal rise, and sea water slowly withdrew westward, forming a set of extensive coastal clastic rocks interbedded with marine carbonate rocks [39,40]. The middle Triassic to Jurassic sediments in the Jianghan Basin were mainly terrestrial conglomerate, sandstone, and mudstone; interbedded with coal seams formed from the Carboniferous to early Triassic [41,42]. Under the influence of the Yanshanian movement, a NW-trending fault belt was formed in the Jianghan Basin from the late Jurassic to the early Cretaceous [34]. From the late Cretaceous to the Paleogene, the Jianghan Basin experienced

the active upwelling of the upper mantle induced by the rolling of the Pacific plate and the Indo-Asian collision, resulting in multistage rifting and the formation of extensive siliceous clasts, evaporites, and a large number of basalts in the basin, finally forming the present geographical characteristics [43,44].

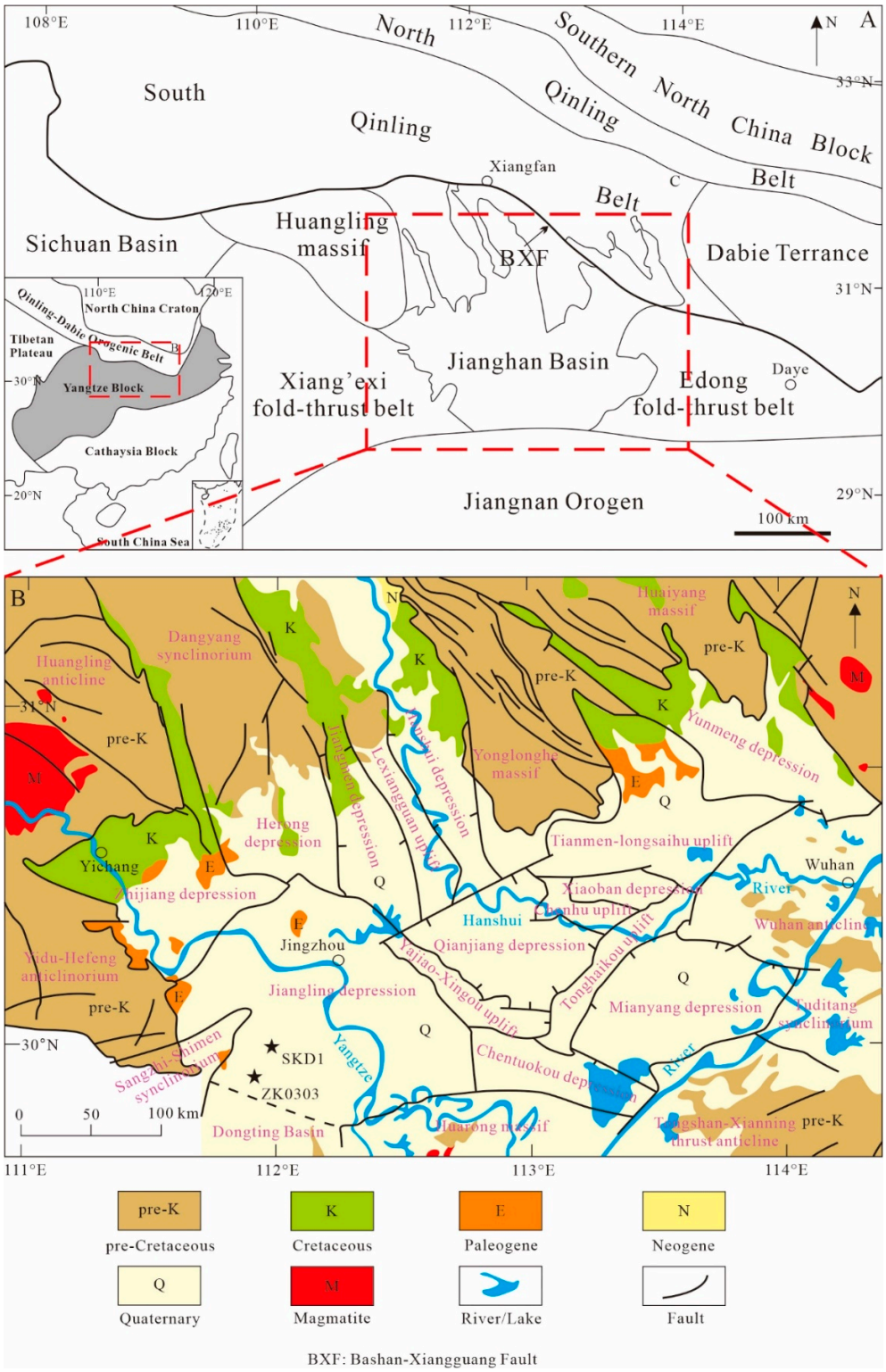

Figure 1. Geologic and tectonic sketch maps of Jianghan Basin region. (**A**) Modified after Wu et al. (2017) [37]. (**B**) Detailed geological map of Jianghan Basin. The black stars represent the well.

The Jianghan Basin is composed of several secondary structural units and depressions. The Jiangling depression is the largest secondary negative tectonic unit in the Jianghan Basin, which was formed on the Yanshanian fold basement under the depression setting of the late Cretaceous to the Paleogene (Figure 1B). The growth and development of the Jiangling depression is controlled by the Qingshuikou fault, the Jishansi fault, the Wen'ansi fault, and the Gongan-Songzi fault, and is divided into two independent units by the Wancheng fault [1,45,46] (Figure 2). In 2016, we obtained a 2302.03 m long well core (ZK0303) in the southwest of the Jiangling depression. The core is mainly composed of purplish pink silty mudstone and dark gray mudstone, interbedded with anhydrite, glauberite, and halite. According to the existing palynological records and a stratigraphic correlation study of the adjacent well, it is preliminarily believed that the boundary between the Paleocene and Eocene is around the 680 m mark of the drilling core [47].

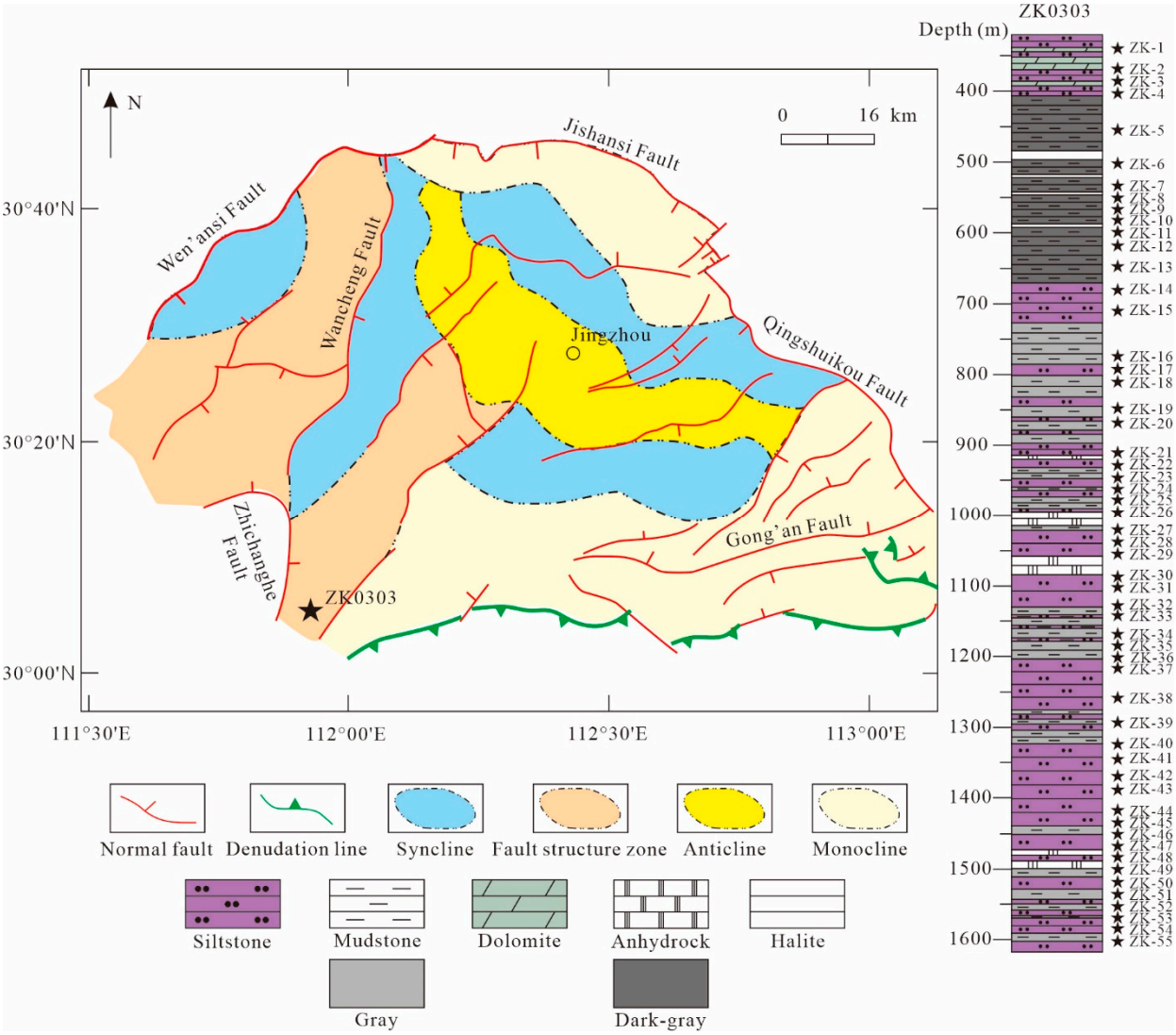

Figure 2. Tectonic map of Jiangling depression (modified after Teng et al., 2019 [33]), and stratigraphic column of well ZK0303.

3. Sampling and Methods

3.1. Analyses of Major and Trace Elements

A total of 55 samples were collected from Well ZK0303 based on the criteria of vertical differences, changes in sediment color, particle size, and physical properties (Figure 2). We split core ZK0303 into two halves in the longitudinal direction, and selected the fresh part

that was not contaminated. All samples were stored in plastic bags to avoid secondary pollution and oxidation as much as possible. Before the geochemical analysis all samples were air-dried, crushed to 200 mesh and thoroughly mixed. The major elements were analyzed using X-ray fluorescence spectrometer (XRF), and the analytical accuracy was estimated at 1% for SiO_2 and 2% for the other oxides. The trace and rare earth elements were tested via inductively coupled plasma mass spectrometry (ICP-MS), and the analytical uncertainties were estimated at approximately 10% and 5% for trace and rare elements with abundances of <10 ppm and >10 ppm, respectively.

Before the experiment, the samples were crushed in an agate mortar to less than 200 mesh. After that, the powdered samples were heated and poured into a mixture of anhydrous lithium tetraborate, lithium fluoride, and ammonium nitrate to melt into glass sheets, which continued to be heated in a muffle furnace to determine loss on ignition. Finally, the fused samples were heated to 800 °C and analyzed using a sequential wavelength dispersive X-ray fluorescence spectrometer (AB104L, Axios-mAX, Malvern Panalytical, Almelo, The Netherlands). The detailed calibrations can be found in Lang et al. (2018) [48].

The trace earth element content was measured via inductively coupled plasma mass spectrometer (ICP-MS, ELEMENT XR). The powdered samples were heated with HF and HNO_3, then evaporated to dryness, and HNO_3 was added to dissolve the samples. Then, HNO_3 was added to the samples again and heated to 130 °C. Finally, distilled water was added to the solution and the trace element content was measured. All geochemical analyses were carried out in the Analytical Laboratory of the Beijing Research Institute of Uranium Geology.

The minimum detection limit (MDL) of all elements can be found in Supplementary Table S1.

3.2. Indicators of Paleoclimate and Paleoenvironment

The elemental geochemistry, such as FeO/MnO and Al_2O_3/MgO, is a good indicator of paleoclimate changes [49–51]. This is because Mn content is relatively high in an arid environment, while the opposite is true in a humid environment; Fe precipitates quickly in the form of an Fe(OH) colloid in humid environments [52]. Worash (2002) [53] found that the distribution, composition, and relative concentration of some trace elements in mudstone may indicate the paleoclimate and palaeoenvironment. Zhao et al. (2007) [54], and Cao et al. (2012) [55], proposed using the C-value as an indicator of paleoclimate. The calculation formula of the C-value is as follows: C-value = ∑(Fe + Mn + Cr + V + Ni + Co)/∑(Ca + Mg + Sr + Ba + K + Na). This is because the Fe, Mn, Cr, V, Ni, and Co elements are relatively enriched in humid conditions, while in arid conditions, evaporation precipitates saline minerals, resulting in the concentration of Ca, Mg, K, Na, Sr, and Ba elements.

In an arid climate, source rocks are dominated by physical weathering, in which they can only be mechanically broken down into smaller grain sizes without significant changes in mineralogical and chemical composition [56]. Chemical weathering plays a dominant role in humid climates and strongly controls the major and trace element composition of siliceous clastic sediments [21,57–60]. It directly affects the removal of mobile elements (Na, K, Ca) and the enrichment of immobile elements (Al, Si) in the sediments [21]. The chemical index of alteration (CIA = $Al_2O_3/(Al_2O_3 + CaO^* + Na_2O + K_2O) \times 100$ [61]; $CaO^* = CaO - 10/3 \times P_2O_5$ [59]) can determine the mobility of elements during chemical weathering and potassium metasomatism during diagenesis, and evaluate the weathering history and source rock composition. The chemical index of weathering (CIW = $Al_2O_3/(Al_2O_3 + CaO + Na_2O) \times 100$ [57]), and the plagioclase index of alteration (PIA = $100 \times (Al_2O_3 - K_2O)/(Al_2O_3 + CaO^* + Na_2O - K_2O)$ [60]), are also important bases for assessing source area paleoweathering. The higher the values of CIA, CIW, and PIAc, the stronger the chemical weathering in the source area [21].

The solubility of trace elements such as U, Ni, V, Mo, and Co is controlled by the redox conditions, so they are generally enriched in sediments formed in reducing environments [24,62–64]. In a sedimentary environment, they are easily soluble under oxic

conditions. During diagenesis, trace elements are practically immobile and maintain the original record of deposition, so they can be used as a standard index to reconstruct the redox environment of ancient water [65]. In their study of the late Jurassic redox environment in northwestern Europe, Jones and Manning (1994) [66] concluded that the ratios of U/Th, Ni/Co, and V/Cr are reliable substitutes for redox conditions. In general, high ratios of U/Th, Ni/Co, and V/Cr indicate an anoxic environment, while low ratios indicate an oxic environment.

Some trace elements, such as the Sr/Ba ratio [67–69], are very sensitive to changes in salinity, so they can be used to indicate paleosalinity. In general, with an increase in salinity, Sr and Ba are precipitated by the formation of sulfate, but $BaSO_4$ preferentially precipitates first. When $BaSO_4$ is completely precipitated, $SrSO_4$ begins to precipitate.

4. Results

4.1. Major Elements Geochemistry

Among the major elements, the SiO_2 (15.65–58.40 wt.%, average 44.22 wt.%), Al_2O_3 (4.14–17.58 wt.%, average 13.24 wt.%), and CaO (3.85–19.37 wt.%, average 8.84 wt.%) are the top three by content (Supplementary Table S1). The content of Fe_2O_3 (1.65–7.05 wt.%, average 5.07 wt.%), MgO (2.02–8.09 wt.%, average 4.75 wt.%), and K_2O (1.10–4.83 wt.%, average 3.29 wt.%) is each more than 1%. The content of Na_2O and FeO is around 1 wt.% each, and the content of TiO_2, MnO, and P_2O_5 is each less than 1 wt.% each. The major element content of all samples was allocated according to the average post-Archean Australian shale (PAAS); almost all the SiO_2, Al_2O_3, Fe_2O_3, TiO_2, and MnO content in Well ZK0303 was lower than PAAS (Figure 3A). In contrast, the content of all CaO and MgO, and most of Na_2O, was higher than those of PAAS and show strong enrichment (Figure 3A).

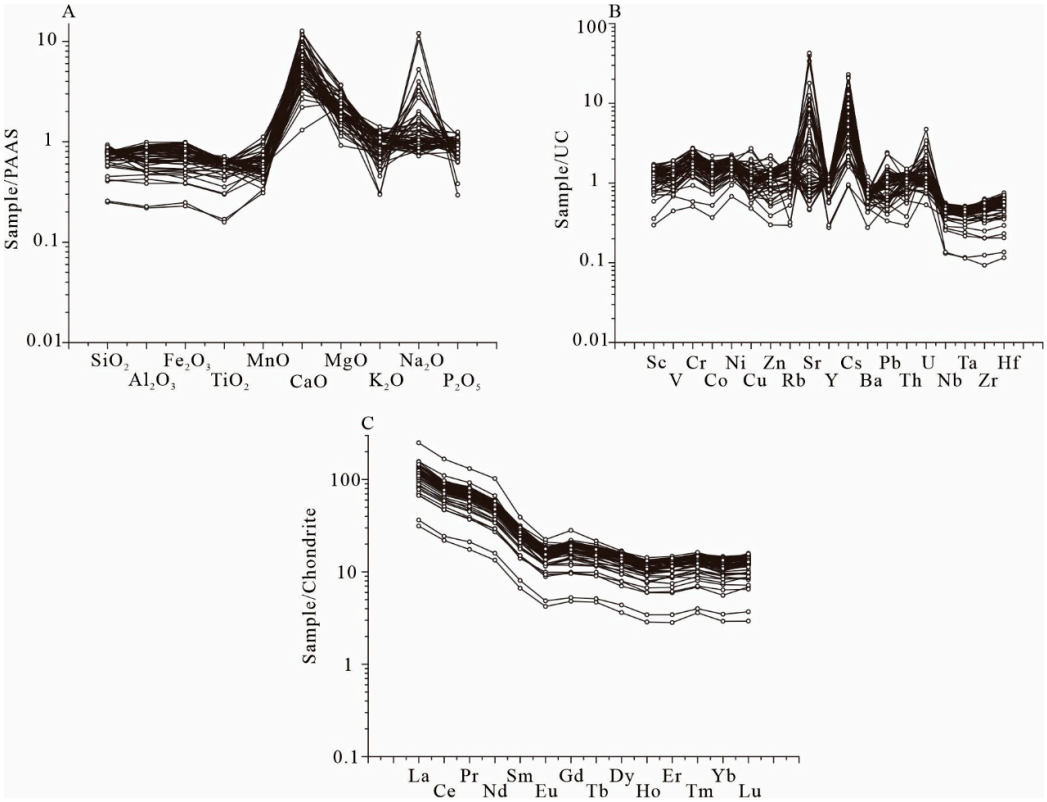

Figure 3. (**A**) PAAS-normalized major element diagram of samples from Well ZK0303, data of PAAS are from McLennan, 1989 [70]; (**B**) UC-normalized trace-element diagram of samples from Well ZK0303, data of the UC are from Taylor and McLennan, 1985 [71]; (**C**) chondrite-normalized rare element diagram of samples from Well ZK0303, data of the chondrite are from Boynton, 1984 [72].

4.2. Trace and Rare Elements Geochemistry

The three elements with the highest average content are Sr (161.0–14,887.0 ppm); Ba (152–656 ppm); and Rb (33.0–225.0 ppm), and their average contents are 2044.8 ppm; 383.9 ppm; and 144.6 ppm, respectively (Supplementary Table S1). The content of U (1.5–13.2 ppm, average 4.2 ppm); Hf (0.7–4.4 ppm, average 3.0 ppm); and Ta (0.3–1.1 ppm, average 0.9 ppm) is the lowest. The preservation state of each element varies greatly if they are normalized to upper crust (UC) data. The content of Sr and Cs is enriched relative to UC, the content of Nb, Ta, Zr, and Hf show strong depletion (Figure 3B).

For REE, the Ce content ranges from 17.5 to 88 ppm, averaging 62.51 ppm; the La content ranges from 9.4 to 74.7 ppm, averaging 35.11 ppm; and the Nd content ranges from 8.04 to 61.40 ppm, averaging 29.34 ppm (Supplementary Table S1). They are the three most abundant REEs. The LREE/HREE ratios range from 7.70 to 13.83, averaging 8.93. In the chondrite-normalized diagram (Figure 3C), all samples show a set of steep dips in the light REE (LREE) curves, whilst the curves of the heavy REE (HREE) are flat. The V-shaped Eu pattern in the standardized diagram represents negative anomalies.

4.3. Change Trends of Element Ratios

In Figure 4 and Supplementary Table S2, the ratios of FeO/MnO, Al_2O_3/MgO, C-value, CIA, CIW, and PIA have similar changing trends. From 1599.5 to 853 m, the ratios of FeO/MnO, Al_2O_3/MgO, and the C-value fluctuate in a large range, and the change frequencies are high. The change trends of the CIA, CIW, and PIA range are similar to the FeO/MnO, Al_2O_3/MgO, and C-value. From 853 to 650 m, the ratios of FeO/MnO are low except for the high at 779.5 m, and the ratios of Al_2O_3/MgO, C-value, CIA, CIW, and PIA are high except for the low at 809.9 m. From 650 to 363 m, the change trend of FeO/MnO is relatively stable; however, there is a significant decrease at 400.5 m. The ratios of Al_2O_3/MgO, C-value, CIA, CIW, and PIA are in the low range from 650 to 363 m, but significantly increase at 550 m and 400.5 m. At 339 m, the ratios of C-value, CIA, CIW, and PIA values increase, but the ratios of FeO/MnO and Al_2O_3/MgO decrease.

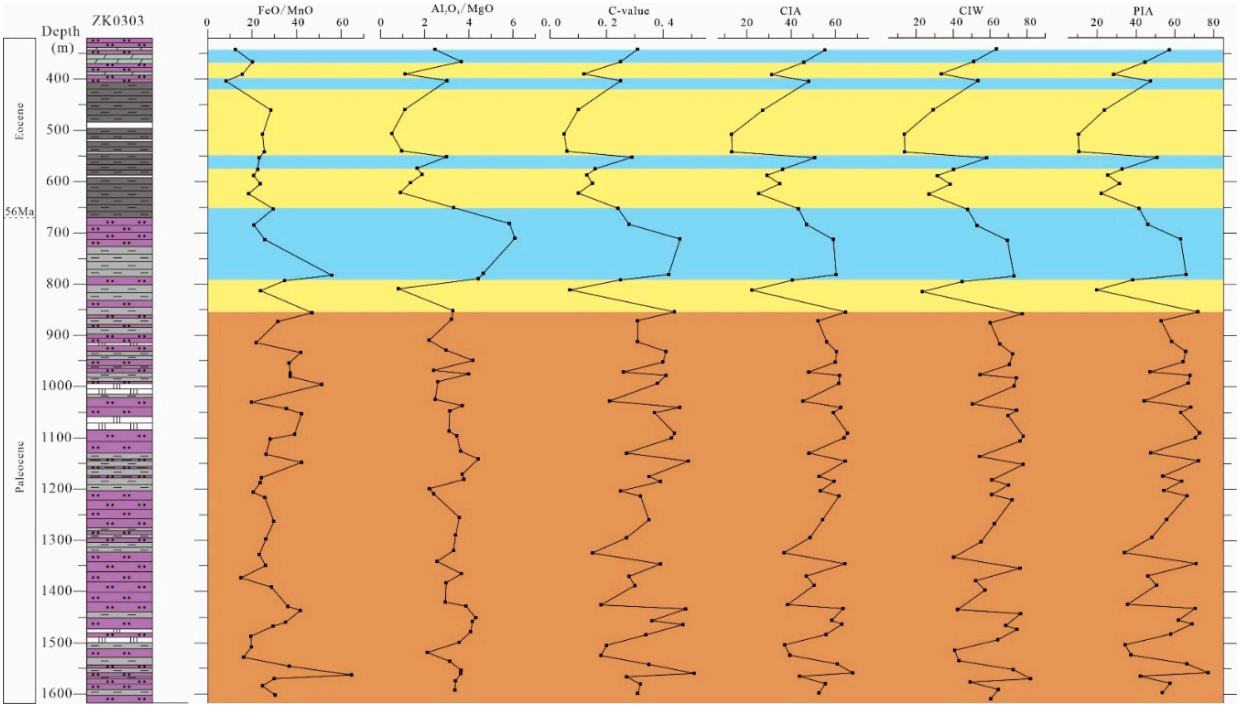

Figure 4. Distribution diagram of major and trace element ratios from well ZK0303, Jiangling depression (Legend as in Figure 2). Brown areas represent semi-humid to semi-arid environments, light yellow areas represent arid environments, and light blue areas represent humid environments.

In Figure 5 and Supplementary Table S2, the values of Ni/Co, V/Cr, and U/Th in the section from 1599.5 to 853 m are generally low, while the values in individual sediments are high. From 853 to 650 m, the ratios of Ni/Co, V/Cr, and U/Th are low except for the high at 809.9 m (Figure 5). From 650 to 339 m, the ratio of Ni/Co is high except for the low at 550, 400.5, and 339 m; the ratios of V/Cr and U/Th are high except for the low at 573, 400.5, and 363 m (Figure 5). From 1599.5 to 853 m, the ratio of Sr/Ba experiences multiple increases. From 853 to 650 m, the ratio of Sr/Ba is low except for the high at 809.9 m (Figure 5). From 650 to 339 m, the change trend of Sr/Ba is similar to V/Cr and U/Th (Figure 5).

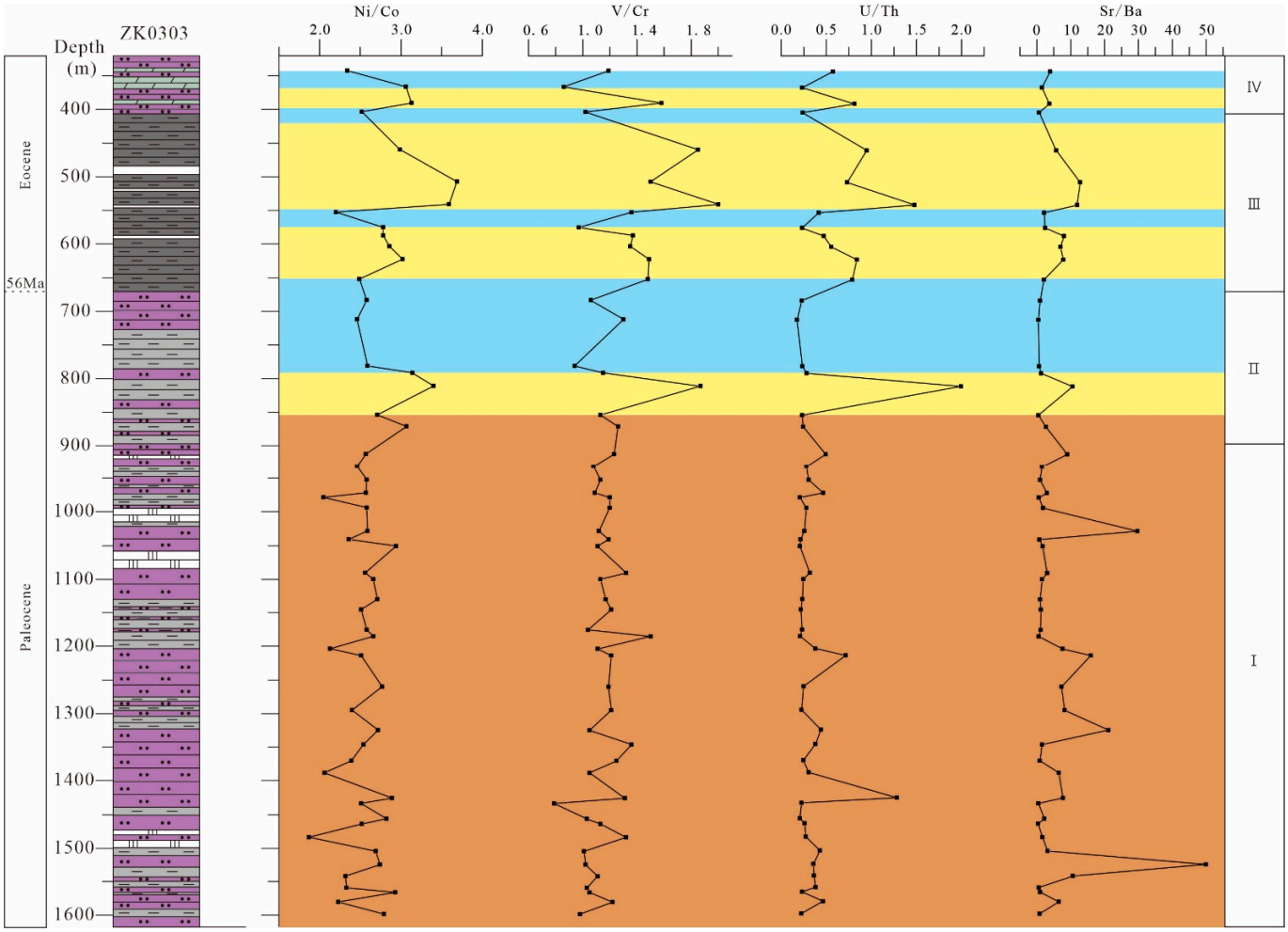

Figure 5. Distribution diagram of trace element ratios from well ZK0303, Jiangling depression (Legend as in Figure 2). Brown areas represent semi-humid to semi-arid environments, light yellow areas represent arid environments, and light blue areas represent humid environments. Stage I: playa-lake, Stage II: brackish lake, Stage III: saline lake, Stage IV: brackish playa lake.

In order to verify the reliability of the above chemical indicators, principal component analysis was carried out on the data. In Figure 6, climate indicators (FeO/MnO, C-value) and chemical weathering indicators (CIA, CIW, and PIA) are in the same quadrant, indicating a clear positive correlation between them. Al_2O_3/MgO, which is also a climate indicator, is not in the same quadrant as FeO/MnO, C-value, CIA, CIW, and PIA, but they are not far apart and on the same side, which indicates that although the correlation is not high, they still have similar trends. Therefore, a change in FeO/MnO and C-value should be paid attention in the identification of climate. Sr/Ba, which indicates salinity, is in opposition to climate indicators (FeO/MnO, C-value) and chemical weathering indicators (CIA, CIW, and PIA), indicating that salinity decreases with increasing humidity and chemical

weathering. Ni/Co, V/Cr, and U/Th are all in the same quadrant, indicating that the redox condition indicators have good reliability.

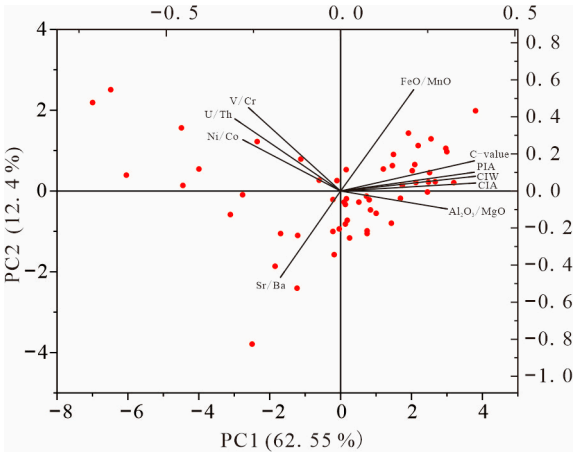

Figure 6. Principal component analysis diagram of selected element ratios. Most samples are located in range of chemical weathering indicators (CIA, CIW and PIA) and paleoclimatic indicators (Al_2O_3/MgO).

5. Discussion

5.1. Paleoclimate and Paleoweathering

High ratios of FeO/MnO, Al_2O_3/MgO, and C-value in the sediment correspond to a humid climate, while low value is a response to an arid climate [49,50,54]. The complex variation trends of FeO/MnO, Al_2O_3/MgO, and C-value indicate that the climate in the Jiangling depression during the early–middle Paleocene was very unstable and changed rapidly between aridity and humidity, so the climate type should have been semi-humid and semi-arid. However, *Ephedripites* and *Ulmaceae* dominate the pollen assemblages of the Jianghan Basin during the early–middle Paleocene, reflecting a dry and warm climate [7]. The $\delta^{13}C$ and $\delta^{18}O$ of carbonates also indicate that the climate of the Jianghan Basin during the Paleocene was dry and hot, and changed to humid in the Eocene [1]. The palynological data of Sun and Wang (2005) [7] came from the summary of complex data, while the $\delta^{13}C$ and $\delta^{18}O$ data of Wang et al. (2013) [1] came from evaporite section, so they could not reflect the whole Paleocene climate. The increases of FeO/MnO, Al_2O_3/MgO, and C-value ratios in the Jianghan Basin during late Paleocene–early Eocene reflect the humid climate characteristics at that time. The ratios of FeO/MnO, Al_2O_3/MgO, and C-value in the Jianghan Basin during Eocene are low on the whole, but have increased many times. This indicates that although the climate of the Eocene was generally arid, it became humid several times. Although the Eocene climate was arid enough to allow the deposition of halite, it experienced short periods of humidity (Figure 4). The temperature data of the Eocene halite fluid inclusion of the Jianghan Basin reflect the existence of high temperatures when the halite was deposited [19,20], and the $\delta^{13}C$ and $\delta^{18}O$ of the whole evaporite section indicate that there was a humid climate during the interval of halite deposition [1]. These conclusions are consistent with the reconstructed Eocene climate of the Jiangling depression in this study.

The cause of the semi-humid to semi-arid climate of the Paleocene in the Jianghan Basin may be related to the instability of subtropical highs controlled by the planetary wind system [73–75]. This significant climate change during the late Paleocene to early Eocene appears to be potentially linked to the PETM. During the PETM, the global water cycle changed, which also led to an increase in precipitation in the Jianghan Basin [16,17]. One interpretation is that the arid climate and the frequent short periods of humidity of the Eocene may be related to the instability of the subtropical highs. Alternatively, they may be related to hyperthermals after the PETM, such as ETM2, H2, I1, and I2 [15,76,77].

From 1599.5 to 853 m, the ratios of CIA, CIW, and PIA rapidly changed between low and high values (Figure 4), indicating that chemical weathering of the Jiangling depression was unstable in the early to middle Paleocene. From 853 to 650 m, the ratios of CIA, CIW, and PIA experienced a dramatic shift from low to high (Figure 4). This suggests that chemical weathering increased rapidly from low intensity to high intensity during the late Paleocene to early Eocene. The variation trends of chemical weathering indicators (CIA, CIW, and PIA) from 650 to 339 m indicate that the intensity of chemical weathering was low in the Eocene, but experienced several increases. The fluxes of precipitation and water promote mineral dissolution by providing water to mineral surfaces in regolith, reducing the concentration of mineral dissolution in regolith pore water, and drive the net dissolution reaction forward [78]. An increase in humidity and temperature will accelerate the rate of chemical weathering [79–82]. Sheldon et al. (2002) [83] reported that the degree of chemical weathering increases with precipitation. In Figure 4, the indicators of chemical weathering (CIA, CIW, and PIA) and humidity (FeO/MnO, Al_2O_3/MgO, and C-value) showed a similar change trend, which may indicate that the increase in humidity led to intensification of the degree of lake sediment chemical weathering in the Jiangling depression. The most intense period of chemical weathering of sediments in the Jiangling depression was during the PETM (Figure 4). Korasidis et al. (2022) [84] argued that the precipitation of high latitudes increased, and the middle to low latitudes became arid during the PETM. The latitude of the Jiangling depression during the PETM was about 21.25° north [85], so the climate at that time should have been dry. However, Xie et al. (2022) [17] believed that higher temperatures produced stronger ocean–land thermal contrast, transporting abundant moisture from the tropical oceans to East Asia, and that the strengthened hydrological cycle in response to elevated temperature counterbalanced the negative impact of the lower Tibetan Plateau on precipitation. Climate simulations suggest that an active atmospheric river stretched from the tropical proto-Indian Ocean, transporting plentiful oceanic moisture to East Asia during the PETM [86]. The above factors led to the significant increase of precipitation in the Jiangling depression during the PETM, which also greatly enhanced the degree of chemical weathering of sediments.

5.2. Redox Conditions

According to the changing trends of U/Th, Ni/Co and V/Cr from 800 to 339 m, the Eocene lake was oxic during a humid climate, but the lake was in reducing condition during an arid climate. The reason for this phenomenon may be that the lake was in a closed still water environment; because the external recharge was reduced during the dry period, the water body was stratified and the bottom of the lake was anoxic, creating reducing conditions in the sediment [66]. When the climate became humid, the lake accepted the replenishment of the external water body and became open; this made the lake water rich in oxygen, so most of the sediment at the bottom of the lake was in oxic conditions. The rapid changes between an arid and humid climate in the Paleocene allowed the lake to receive frequent replenishment from external water bodies, so that the sediments were almost in oxic conditions, except for during extremely arid climates (such as the significant aridity recorded at 809.9 m).

5.3. Paleosalinity

The most direct and effective way to distinguish lake salinity is to identify sedimentary sequences, especially in salt lake sedimentary systems. According to lithology, grain size, and sedimentary structure, the 320–1600 m section of well ZK0303 is divided into four main lake facies types: playa lake, shallow to semi-deep brackish lake, deep saline lake, and brackish playa lake (Figures 7 and 8).

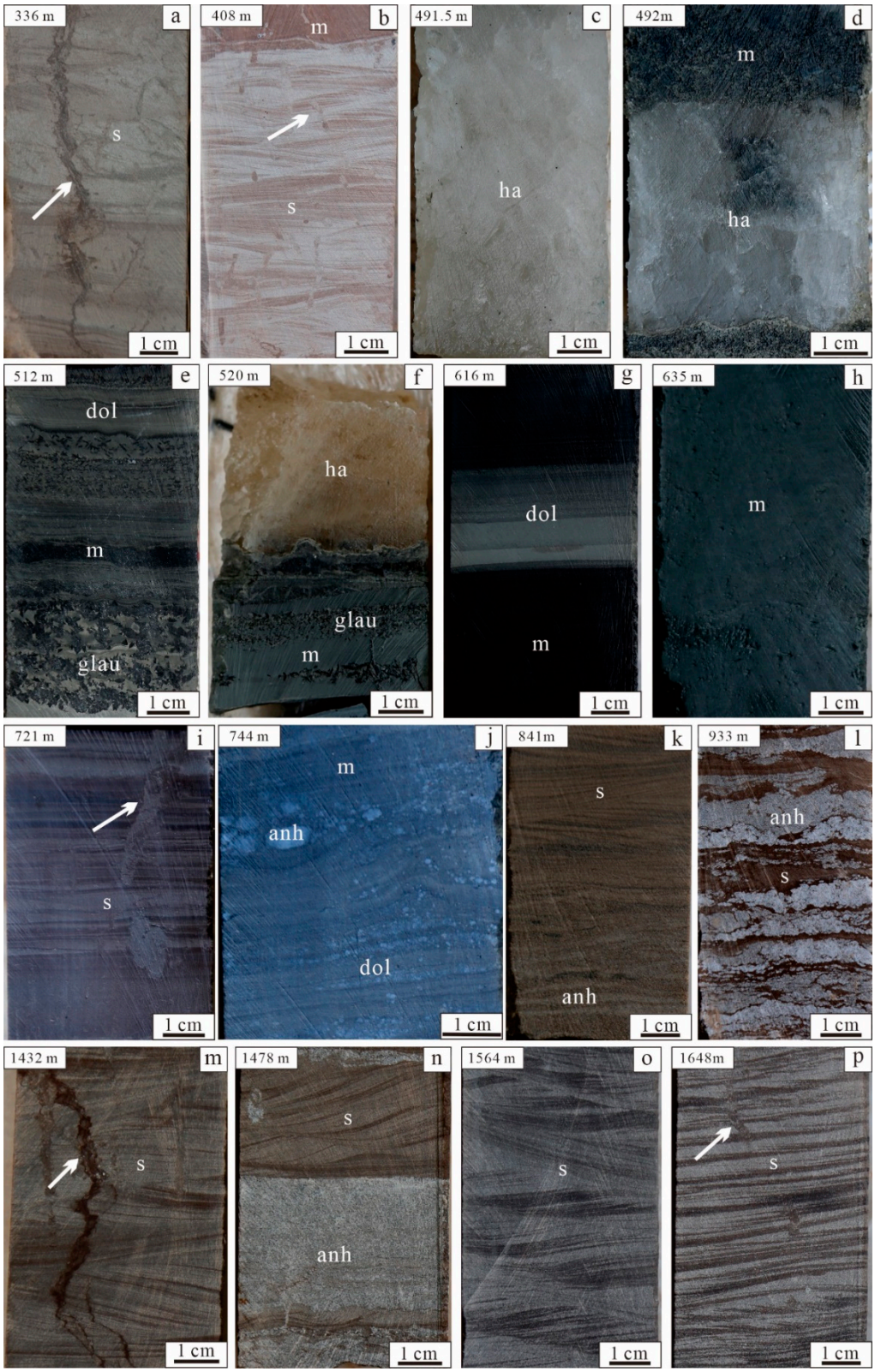

Figure 7. Photographs of major sedimentary structures in 320–1600-m segment of well ZK0303. (**a**) Mud crack (white arrow); (**b**) wavy cross-bedded siltstone, burrow (white arrow); (**c**) massive halite; (**d**) conformable contact of halite and organic matter-rich mudstone*; (**e**) mudstone interbedded with dolomite and glauberite; (**f**) conformable contact of halite, glauberite and mudstone*; (**g**) organic matter-rich mudstone interbedded with layered dolomite; (**h**) massive mudstone*; (**i**) cross-bedded siltstone, burrow (white arrow); (**j**) thin-layer dolomite and banded anhydrite; (**k**) cross-bedded siltstone and thin-layer anhydrite; (**l**) siltstone interbedded with anhydrite; (**m**) cross-bedded siltstone

and mud crack (white arrow); (**n**) herringbone cross-bedded and bedded anhydrite; (**o**) herringbone cross-bedded siltstone; and (**p**) parallel-bedded siltstone, burrow (white arrow). Depth indicator for each panel corresponds to middle of panel. All photographs are oriented vertically. m: mudstone; s: siltstone; ha: halite; dol: dolomite; glau: glauberite; anh: anhydrite. * potential hydrocarbon source rocks.

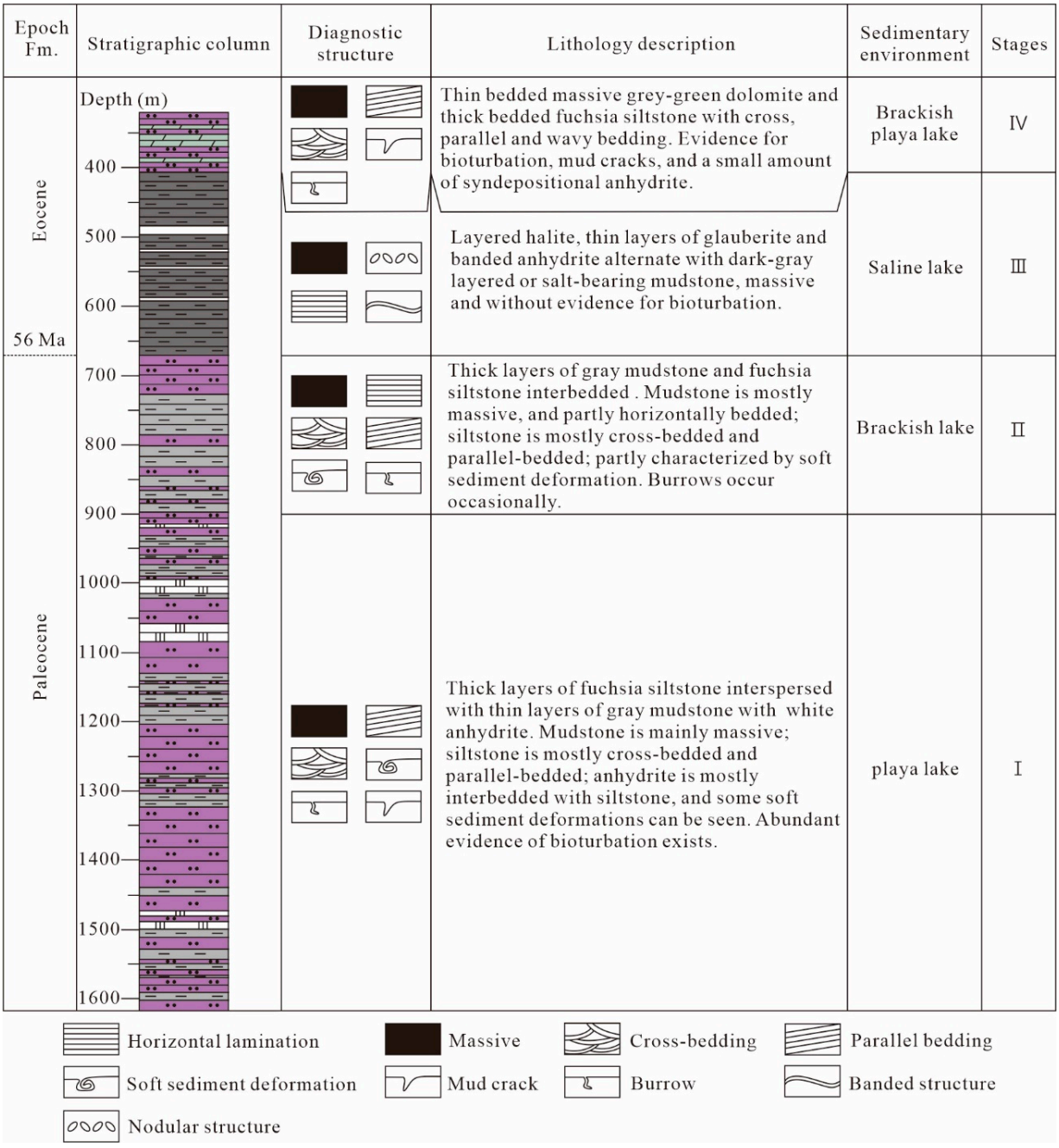

Figure 8. Lithofacies in 320 to 1600 m section of well ZK0303 (Legend as in Figure 2).

5.3.1. Playa Lake (Stage I)

Rocks are mainly composed of thick layers of mostly coarse-grained fuchsia-red siltstone, partly interbedded with grey mudstone and bedded white anhydrite (Figures 7 and 8). Bioturbation traces such as burrows and signs of exposure such as mud cracks occur in this section (Figure 7m,n,p). There are cross bedding, herringbone cross bedding and parallel

bedding in the siltstones (Figure 7n–p). The mostly relatively coarse grain size and the cross bedding indicate flowing waters, and the burrows and mud cracks show that the sediments were accumulated in shallow, well-oxygenated waters and were exposed from time to time.

5.3.2. Brackish Lake (Stage II)

Mudstone and siltstone units are interbedded, and thin layers of anhydrite appear sporadically (Figures 7 and 8). In this section, mud cracks formed in the exposed environment are not observed, and only a few bioturbation traces appear (Figure 7i). Siltstone and mudstone are mainly massive, and some sandstones are cross or parallel bedded (Figure 7i,l), while a small amount of mudstone is horizontally bedded (Figure 7j). Horizontal bedded and bioturbation traces indicate a relatively calm semi-deep lake environment, while coarse-grained siltstone interbedded with fine-grained mudstone and cross bedding indicates a shallow lake environment and a dynamic hydrological environment with flow.

5.3.3. Saline Lake (Stage III)

This section is dominated by fine-grained dark gray mudstone, containing dolomite, anhydrite, glauberite, and halite (Figures 7 and 8). The mudstones are mostly massive (Figure 7h), and they are partly horizontally bedded, or interbedded with banded anhydrites, thin layers of glauberite, or halite (Figure 7e,g). In this section, the evidence for bioturbation or mud cracks was not observed. The horizontal bedding results from sediment accumulation in a stable calm environment.

5.3.4. Brackish Playa-Lake (Stage IV)

Characteristics similar to those in the section between 1200–1600 m occur in the uppermost sequence of the core again, indicating the reestablishment of a playa-lake environment (Figures 7 and 8). However, in addition to siltstone, it is mainly dolomite, and anhydrite clumps are occasionally seen.

The climate of the Jiangling depression was in rapid alternations of aridity and humidity during the early and middle Paleocene (Figure 5). In an arid climate, evaporation increases the salinity of the lake, and gypsum deposited, but when the climate becomes humid, the salinity of the lake decreased due to weaker evaporation and increased recharge. Therefore, the salinity of lake water varied greatly in the early to middle Paleocene (stage I). The late Paleocene climate changed from an ephemeral extreme aridity to a long period of humidity (Figure 5), so the salinity of the lake water decreased (stage II). In the Eocene, the climate of the Jiangling depression was mainly arid (Figure 5), the salinity of the lake increased and halite was precipitated (stage III). Finally, as the climate became more humid, the lake became less saline (stage IV). The changes of climate also appear to have influenced the sediment input of the paleo-saline lake in the Jiangling depression. The transport dynamics of suspended sediment in small headwater catchments contribute a great deal to sediment generation and delivery to downstream reaches, and thus determine the sediment budgets of large river basins [87–89]. Rainfall-runoff events are the most important factors determining suspended sediment transport [90–92]. The alternations of aridity and humidity in the Jiangling depression during the early to middle Paleocene resulted in unstable sediment input, with large sediment input in the humid period resulting in coarse-grained siltstone formation, and limited sediment input in the arid period resulting in mudstone formation (Stage IV). The climate changed rapidly from arid to humid during the late Paleocene–early Eocene, and sediment input increased, resulting in a transition from mudstone to siltstone (Stage III). The long-term dry period in the Eocene resulted in low sediment input, and the lithology was mainly mudstone (stage II). However, the short-term strong humid climate increased the sediment input, and eventually siltstone was formed (stage I).

A high Sr/Ba ratio indicates a higher water salinity [66]. The sedimentary sequences and Sr/Ba ratio show that the climate of the Jiangling depression greatly controlled the

salinity of lake water during the Paleocene to the Eocene. The climate in the early and middle Paleocene alternated frequently between aridity and humidity, and the salinity of the lake varied greatly. During the late Paleocene–early Eocene, the climate changed from arid to humid, and the salinity of the lake water also changed from increasing to decreasing. In the Eocene, the climate was mainly arid, and the salinity of the lake increased, but with the onset of a humid climate, the salinity of the lake would decrease again.

6. Conclusions

According to the chemical characteristics of major and trace elements, we reconstructed the environment of the Paleocene–Eocene saline lake in the Jiangling depression, southwestern Jianghan Basin, and obtained the following conclusions:

(1) The Jiangling depression experienced a semi-humid to semi-arid climate during the early–middle Paleocene. There was a rapid shift to a humid climate during the PETM, following a short period of intense dryness. In the Eocene, the climate was arid, but it experienced short periods of humidity. The trend of chemical weathering is similar to that of climate change. The instability of subtropical highs controlled by the planetary wind system, and hyperthermals (such as PETM) may be important factors in climate change.

(2) The climate of the Jiangling depression underwent frequent fluctuations between humid and arid conditions during the Paleocene–Eocene. In the humid periods and alternations of aridity and humidity, the lake received external water, resulting in a weak stratification of the lake water, so sediments were formed under oxic conditions. In the arid phase, the lake became a still water environment, leading to reducing conditions for sedimentation.

(3) Under the control of climatic conditions, the salinity of the lake changed greatly in the early–middle Paleocene. From the late Paleocene to the early Eocene, the overall salinity of the lake was low; in the Eocene, the salinity of the lake increased, but there were still several decreases.

Supplementary Materials: The following supporting information can be downloaded at https://www.mdpi.com/article/10.3390/min14030234/s1, Table S1: Major, trace and rare elements from the samples of well ZK0303, Jiangling depression; Table S2: Selected element ratios from samples of well ZK0303, Jiangling depression.

Author Contributions: K.Y. and C.W. designed the research and prepared the original manuscript. J.W., R.C. and L.L. revised the manuscript. R.L. participated in sample collection and processing. All authors have read and agreed to the published version of the manuscript.

Funding: This work was supported by the National Natural Science Foundation of China (Nos. U20A2092, 42002106, 41907262 and 41502089); the Central Public Welfare Scientific Research Basic Scientific Research Business Expenses (No. KK2005); the National Basic Research Program of China (973 program) (No. 2011CB403007); and the China Geological Survey (No. DD20190606).

Data Availability Statement: Data are contained within the article or Supplementary Materials.

Acknowledgments: We are grateful to reviewers for their critical and constructive review.

Conflicts of Interest: The authors declare no conflicts of interest.

References

1. Wang, C.L.; Liu, C.L.; Xu, H.M.; Wang, L.C.; Zhang, L.B. Carbon and oxygen isotopes characteristics of Paleocene saline lake facies carbonates in Jiangling depression and their environmental significance. *Acta Geosci. Sin.* **2013**, *34*, 567–576.
2. Wang, C.L.; Yu, X.C.; Li, R.Q.; Yan, K.; You, C. Origin of lithium-potassium brines in the Jianghan Basin, South China: Constraints by water-rock reactions of Mesozoic-Cenozoic igneous rocks. *Minerals* **2021**, *11*, 1330. [CrossRef]
3. Liu, C.L. Characteristics and formation of potash deposits in continental rift basins: A review. *Acta Geosci. Sin.* **2013**, *34*, 515–527.
4. Shen, L.J.; Liu, C.L.; Xu, H.M.; Wang, C.L.; Wang, L.C.; Liu, B.K.; Zhang, L.B. Paleocene mineral assemblage characteristics of Jianghan depression and their significance for potash formation. *Miner. Depos.* **2014**, *33*, 1020–1030.

5. Liu, C.L.; Zhao, Y.J.; Fang, X.M.; Lv, F.L.; Wang, L.C.; Yan, M.D.; Zhang, H.; Ding, T. Plate tectonic control on the distribution and formation of the marine potash deposits. *Acta Geol. Sin.* **2015**, *89*, 1893–1907.
6. Liu, C.L.; Yu, X.C.; Zhao, Y.J.; Wang, J.Y.; Wang, L.C.; Xu, H.M.; Li, J.; Wang, C.L. A tentative discussion on regional metallogenic background and mineralization mechanism of subterranean brines rich in potassium and lithium in south China block. *Miner. Depos.* **2016**, *35*, 1119–1143.
7. Sun, X.J.; Wang, P.X. How old is the Asian monsoon system? Palaeobotanical records from China. *Palaeogeogr. Palaeoclimatol. Palaeoecol.* **2005**, *222*, 181–222. [CrossRef]
8. Guo, Z.T.; Sun, B.; Zhang, Z.S.; Peng, S.Z.; Xiao, G.Q.; Ge, J.Y.; Hao, Q.Z.; Qiao, Y.S.; Liang, M.Y.; Liu, J.F.; et al. A major reorganization of Asian climate by the early Miocene. *Clim. Past* **2008**, *4*, 153–174. [CrossRef]
9. Zachos, J.; Pagani, M.; Sloan, L.; Thomas, E.; Billups, K. Trends, rhythms, and aberrations in global climate 65 Ma to present. *Science* **2001**, *292*, 686–693. [CrossRef]
10. McInerney, F.A.; Wing, S.L. The Paleocene-Eocene thermal maximum: A perturbation of carbon cycle, climate, and biosphere with implications for the future. *Annu. Rev. Earth Planet. Sci.* **2011**, *39*, 489–516. [CrossRef]
11. Kennett, J.P.; Stott, L.D. Abrupt deep-sea warming, palaeoceanographic changes and benthic extinctions at the end of the palaeocene. *Nature* **1991**, *353*, 225–229. [CrossRef]
12. Pagani, M.; Pedentchouk, N.; Huber, M.; Sluijs, A.; Schoutern, S.; Brinkhuis, H.; Damsté, J.S.S.; Dickens, G.R.; Expedition 302 Scientists. Arctic hydrology during global warming at the Palaeocene/Eocene thermal maximum. *Nature* **2006**, *442*, 671–675. [CrossRef]
13. Cui, Y.; Kump, L.R.; Ridgwell, A.J.; Charles, A.J.; Junium, C.K.; Diefendorf, A.F.; Freeman, K.H.; Urban, N.M.; Harding, I.C. Slow release of fossil carbon during the Palaeocene-Eocene Thermal Maximum. *Nat. Geosci.* **2011**, *4*, 481–485. [CrossRef]
14. Chen, Z.L.; Wang, X.; Hu, J.; Yang, S.; Zhu, M.; Dong, X.; Tang, Z.; Peng, P.; Ding, Z.L. Structure of the carbon isotope excursion in a high-resolution lacustrine Paleocene-Eocene thermal maximum record from Central China. *Earth Planet. Sci. Lett.* **2014**, *408*, 331–340. [CrossRef]
15. Chen, Z.L.; Ding, Z.L.; Tang, Z.H.; Wang, X.; Yang, S.L. Early Eocene carbon isotope excursions: Evidence from the terrestrial coal seam in the Fushun Basin, Northeast China. *Geophys. Res. Lett.* **2014**, *41*, 3559–3564. [CrossRef]
16. Teng, X.H.; Wang, C.L.; Liu, C.L.; Yan, K.; Luo, Z. Paleocene-Eocene Thermal Maximum lacustrine sediments in deep drill core SKD1 in the Jianghan Basin: A record of enhanced precipitation in central China. *Glob. Planet. Change* **2021**, *205*, 103620. [CrossRef]
17. Xie, Y.L.; Wu, F.L.; Fang, X.M. A transient south subtropical forest ecosystem in central China driven by rapid global warming during the Paleocene-Eocene Thermal Maximum. *Gondwana Res.* **2022**, *101*, 192–202. [CrossRef]
18. Chen, Z.L.; Ding, Z.L.; Sun, J.M.; Yang, S.L.; Ni, X.J.; Wang, X.; Wang, Y.L.; Zhang, J.Y.; He, W. Freshwater ecosystem collapse and mass mortalities at the Paleocene-Eocene Thermal maximum. *Glob. Planet. Change* **2023**, *227*, 104175. [CrossRef]
19. Li, H.N.; Wang, C.L.; Liu, C.L.; Yang, S.G.; Xu, H.M.; Hu, H.B.; Yu, X.C.; Liu, J.L. Paleotemperatures of Early Eocene in the Jiangling depression: Evidence from fluid inclusions in thenardite. *Acta Geol. Sin.* **2015**, *89*, 2019–2027.
20. Li, H.N.; Wang, C.L.; Liu, C.L.; Yang, S.G.; Xu, H.M.; Yu, X.C.; Hu, H.B. A research on early Eocene homogenization temperature of fluid inclusions in halite and its paleoclimatic significance in Jiangling depression. *Miner. Depos.* **2016**, *35*, 1205–1216.
21. Nesbitt, H.W.; Young, G.M. Early Proterozoic climates and plate motions inferred from major element chemistry of lutites. *Nature* **1982**, *299*, 715–717. [CrossRef]
22. Bhatia, M.R.; Crook, K.A. Trace element characteristics of graywackes and tectonic setting discrimination of sedimentary basins. *Contrib. Mineral. Petrol.* **1986**, *92*, 181–193. [CrossRef]
23. McLennan, S.M.; Hemming, S.R.; Taylor, S.R.; Eriksson, K.A. Early Proterozoic crustal evolution: Geochemical and Nd-Pb isotopic evidence from metasedimentary rocks, southwestern North America. *Geochim. Cosmochim. Acta* **1995**, *59*, 1153–1177. [CrossRef]
24. Hetzel, A.; März, C.; Vogt, C.; Brumsack, H.J. Geochemical environment of Cenomanian-Turonian black shale deposition at Wunstorf (northern Germany). *Cretac. Res.* **2011**, *32*, 480–494. [CrossRef]
25. Fang, C.G.; Zhang, C.C.; Huang, N.; Teng, L.; Li, C.H.; Shao, W.; Zeng, M. Geological significance of rare earth elements in marine shale of the upper Permian Dalong Formation in the lower Yangtze region, south China. *Minerals* **2023**, *13*, 1195. [CrossRef]
26. Cullers, R.L. The controls on the major and trace element variation of shales, siltstones, and sandstones of Pennsylvanian-Permian age from uplifted continental blocks in Colorado to platform sediment in Kansas, USA. *Geochim. Cosmochim. Acta* **1994**, *58*, 4955–4972. [CrossRef]
27. Yan, Y.; Xia, B.; Lin, G.; Cui, X.J.; Hu, X.Q.; Yan, P.; Zhang, F.Q. Geochemistry of the sedimentary rocks from the Nanxiong Basin, south China and implications for provenance, paleoenvironment and paleoclimate at the K/T boundary. *Sediment. Geol.* **2007**, *197*, 127–140. [CrossRef]
28. Wang, Z.W.; Wang, J.; Fu, X.G.; Zhan, W.Z.; Armstrong-Altrin, J.S.; Yu, F.; Song, C.Y.; Zeng, S.Q. Geochemistry of the upper Triassic black mudstones in the Qiangtang Basin, Tibet: Implications for paleoenvironment, provenance, and tectonic setting. *J. Asian Earth Sci.* **2018**, *160*, 118–135. [CrossRef]
29. Wanas, H.A.; Assal, E.M. Provenance, tectonic setting and source area-paleoweathering of sandstones of the Bahariya Formation in the Bahariya Oasis, Egypt: An implication to paleoclimate and paleogeography of the southern Neo-Tethys region during early Cenomanian. *Sediment. Geol.* **2021**, *413*, 105822. [CrossRef]

30. Yu, W.; Wang, F.; Gong, L.; Hu, J.L.; Ma, Z.R.; Wang, J.; Wu, J.Y.; Xiao, Y.X. Paleoenvironmental, paleoclimatic, and tectonic implications of the Yanghugou Formation in the western margin of the Ordos Basin, China: Evidence from palynology and elemental geochemical characteristics. *Minerals* **2024**, *14*, 32. [CrossRef]
31. Gilder, S.A.; Keller, G.R.; Luo, M.; Goodell, P.C. Timing and spatial distribution of rifting in China. *Tectonophysics* **1991**, *197*, 225–243. [CrossRef]
32. Yu, X.Q.; Shu, L.S.; Deng, P.; Wang, B.; Zu, F.P. The sedimentary features of the Jurassic-Tertiary terrestrial strata in southeast China. *J. Stratigr.* **2003**, *27*, 224–263.
33. Teng, X.H.; Fang, X.M.; Kaufman, A.J.; Liu, C.L.; Wang, J.Y.; Zan, J.B.; Yang, Y.B.; Wang, C.L.; Xu, H.M.; Schulte, R.F.; et al. Sedimentological and mineralogical records from drill core SKD1 in the Jianghan Basin, Central China, and their implications for late Cretaceous-early Eocene climate change. *J. Asian Earth Sci.* **2019**, *182*, 103936. [CrossRef]
34. Hu, S.; Raza, A.; Min, K.; Kohn, B.P.; Reiners, P.W.; Ketcham, R.A.; Wang, J.; Gleadow, A.J.W. Late Mesozoic and Cenozoic thermotectonic evolution along a transect from the north China craton through the Qinling orogen into the Yangtze craton, central China. *Tectonics* **2006**, *25*, TC6009. [CrossRef]
35. Shen, C.B.; Donelick, R.A.; O'Sullivan, P.B.; Jonckheere, R.; Yang, Z.; She, Z.B.; Miu, X.L.; Ge, X. Provenance and hinterland exhumation from LA-ICP-MS zircon U-Pb and fission-track double dating of Cretaceous sediments in the Jianghan Basin, Yangtze block, central China. *Sediment. Geol.* **2012**, *281*, 194–207. [CrossRef]
36. Li, W.; Lu, S.; Xue, H.; Zhang, P.; Wu, S. The formation environment and developmental models of argillaceous dolomite in the Xingouzui Formation, the Jianghan Basin. *Mar. Pet. Geol.* **2015**, *67*, 692–700. [CrossRef]
37. Wu, L.L.; Mei, L.F.; Liu, Y.S.; Luo, J.; Min, C.Z.; Lu, S.L.; Li, M.H.; Guo, L.B. Multiple provenance of rift sediments in the composite basin-mountain system: Constraints from detrital Zircon U-Pb geochronology and heavy minerals of the early Eocene Jianghan Basin, Central China. *Sediment. Geol.* **2017**, *349*, 46–61. [CrossRef]
38. Wang, C.L.; Yan, K.; Yu, X.C.; Wang, J.Y.; Liu, D.H.; Shen, L.J.; Li, R.Q.; You, C. ^{40}Ar/39Ar Geochronology, Geochemistry and Petrogenesis of the Volcanic Rocks in the Jiangling Basin, China. *Minerals* **2022**, *12*, 1099. [CrossRef]
39. Dai, S.W. Discussion on the regional structural features of Jianghan Basin since the indosinian movement. *J. Geomech.* **1996**, *2*, 80–84.
40. Yao, W.H.; Li, Z.X.; Li, W.X.; Su, L.; Yang, J.H. Detrital provenance evolution of the Ediacaran-Silurian Nanhua foreland basin, South China. *Gondwana Res.* **2015**, *28*, 1449–1465. [CrossRef]
41. Chen, W.T.; Zhou, M.; Zhao, X. Late Paleoproterozoic sedimentary and mafic rocks in the Hekou area, SW China: Implication for the reconstruction of the Yangtze Block in Columbia. *Precambrian Res.* **2013**, *231*, 61–77. [CrossRef]
42. Shu, L.S.; Faure, M.; Wang, B.; Zhou, X.M.; Song, B. Late Palaeozoic-Early Mesozoic geological features of South China: Response to the Indosinian collision events in Southeast Asia. *Comptes Rendus Geosci.* **2008**, *340*, 151–165. [CrossRef]
43. Liu, M.; Cui, X.J.; Liu, F.T. Cenozoic rifting and volcanism in eastern China: A mantle dynamic link to the Indo-Asian collision? *Tectonophysics* **2004**, *393*, 29–42. [CrossRef]
44. Li, X.Y.; Zhu, P.M.; Kusky, T.M.; Gu, Y.; Peng, S.B.; Yuan, Y.F.; Fu, J.M. Has the Yangtze craton lost its root? A comparison between the North China and Yangtze cratons. *Tectonophysics* **2015**, *655*, 1–14. [CrossRef]
45. Yang, C.Q.; Chen, K.Q.; Cheng, Z.Q.; Zhan, H.J. Constituent evolution and exploration potential in Jianghan depression. *Nat. Gas Ind.* **2003**, *23*, 51–54.
46. Yu, X.C.; Liu, C.L.; Wang, C.L.; Xu, H.M. Provenance of rift sediments in a composite basin-mountain system: Constraints from petrography, whole-rock geochemistry, and detrital zircon U-Pb geochronology of the Paleocene Shashi Formation, southwestern Jianghan Basin, central China. *Int. J. Earth Sci.* **2018**, *107*, 2741–2766. [CrossRef]
47. Yan, K.; Wang, C.L.; Liu, C.L.; Mischke, S.; Wang, J.Y.; Yu, X.C. Reconstruction of early Paleogene landscapes and climate in the Jianghan Basin, central China: Evidence from evaporates and palynology. *Palaeogeogr. Palaeoclimatol. Palaeoecol.* **2022**, *601*, 111095. [CrossRef]
48. Lang, X.H.; Liu, D.; Deng, Y.L.; Tang, J.X.; Wang, X.H.; Yang, Z.Y.; Cui, Z.W.; Feng, Y.X.; Yin, Q.; Xie, F.W.; et al. Detrital zircon geochronology and geochemistry of Jurassic sandstones in the Xiongcun district, southern Lhasa subterrane, Tibet, China: Implications for provenance and tectonic setting. *Geol. Mag.* **2018**, *156*, 683–701. [CrossRef]
49. Liu, G.; Zhou, D.S. Application of microelements analysis in identifying sedimentary environment-taking Qianjiang Formation in the Jianghan Basin as an example. *Pet. Geol. Exp.* **2007**, *29*, 307–314.
50. Zhang, T.F.; Sun, L.X.; Zhang, Y.; Cheng, Y.H.; Li, Y.F.; Ma, H.L.; Lu, C.; Yang, C.; Guo, G.W. Geochemical characteristics of the Jurassic Yan'an and Zhiluo Formations in the northern margin of Ordos Basin and their paleoenvironmental implications. *Acta Geol. Sin.* **2016**, *90*, 3454–3472.
51. Pan, S.L.; Jiang, Y.; Kang, J.; Chen, B.; Zhang, S.C.; Sun, G.Q. Analysis of paleoclimate and source of the upper section, lower Ganchaigou Formation, Lenghu No. 7 region, north Qaidam Basin. *Acta Sediment. Sin.* **2021**, *39*, 1292–1304.
52. Curtis, C.D. The aqueous geochemistry of metals in the weathering environment: Strengths and weaknesses in our understanding of speciation and process. *Geol. Mag.* **2018**, *67*, 235–246. [CrossRef]
53. Worash, G. Geochemistry provenance and tectonic setting of the Adigrat sandstone northern Ethiopia. *J. Afr. Earth Sci.* **2002**, *35*, 185–198.
54. Zhao, Z.Y.; Zhao, J.H.; Wang, H.J.; Liao, J.D.; Liu, C.M. Distribution characteristics and applications of trace elements in Junggar Basin. *Nat. Gas Explor. Dev.* **2007**, *30*, 30–33.

55. Cao, J.; Wu, M.; Chen, Y.; Hu, K.; Bian, L.Z.; Wang, L.G.; Zhang, Y. Trace and rare earth elements geochemistry of Jurassic mudstones in the northern Qaidam basin, northwest China. *Chem. Erde-Geochem.* **2012**, *72*, 245–252. [CrossRef]
56. Harnois, L. The CIW index: A new chemical index of weathering. *Sediment. Geol.* **1988**, *55*, 319–322. [CrossRef]
57. Middelburg, J.J.; Van der Weijden, C.H.; Woittiez, J.R.W. Chemical processes affecting the mobility of major, minor and trace elements during weathering of granitic rocks. *Chem. Geol.* **1988**, *68*, 253–273. [CrossRef]
58. McLennan, S.M.; Hemming, S.; McDaniel, D.K.; Hanson, G.N. Geochemical approaches to sedimentation, provenance, and tectonics. *Spec. Pap.-Geol. Soc. Am.* **1993**, *284*, 21–40.
59. Fedo, C.M.; Nesbitt, H.W.; Young, G.M. Unraveling the effects of potassium metasomatism in sedimentary rocks and paleosoils, with implications for paleoweathering conditions and provenance. *Geology* **1995**, *23*, 921–924. [CrossRef]
60. Nesbitt, H.W.; Young, G.M. Prediction of some weathering trends of plutonic and volcanic-rocks based on thermodynamic and kinetic considerations. *Geochim. Cosmochim. Acta* **1984**, *48*, 1523–1534. [CrossRef]
61. Francois, R. A study on the regulation of the concentrations of some trace metals (Rb, Sr, Zn, Pb, Cu, V, Cr, Ni, Mn and Mo) in Saanich Inlet Sediments, British Columbia, Canada. *Mar. Geol.* **1988**, *83*, 285–308. [CrossRef]
62. Arthur, M.A.; Sageman, B.B. Marine black shales: Depositional mechanisms and environments of ancient deposits. *Annu. Rev. Earth Planet. Sci.* **1994**, *22*, 499–551. [CrossRef]
63. Yuri, Z.N.; Eder, V.G.; Zamirailova, A.G. Composition and formation environments of the Upper Jurassic-Lower Cretaceous black shale Bazhenov Formation (the central part of the West Siberian Basin). *Mar. Pet. Geol.* **2008**, *25*, 289–306. [CrossRef]
64. Tribovillard, N.; Algeo, T.J.; Lyons, T.; Riboulleau, A. Trace metals as paleoredox and paleoproductivity proxies: An update. *Chem. Geol.* **2006**, *232*, 12–32. [CrossRef]
65. Jones, B.; Manning, D.A.C. Comparison of geochemical indices used for the interpretation of palaeoredox conditions in ancient mudstones. *Chem. Geol.* **1994**, *111*, 111–129. [CrossRef]
66. Meng, Q.T.; Liu, Z.J.; Bruch, A.A.; Liu, R.; Hu, F. Palaeoclimatic evolution during Eocene and its influence on oil shale mineralisation, Fushun Basin, China. *J. Asian Earth Sci.* **2012**, *45*, 95–105. [CrossRef]
67. Jia, J.L.; Liu, Z.J.; Bechtel, A.; Strobl, S.A.I.; Sun, P.C. Tectonic and climate control of oil shale deposition in the Upper Cretaceous Qingshankou Formation (Songliao Basin, NE China). *Int. J. Earth Sci.* **2013**, *102*, 1717–1734. [CrossRef]
68. Fu, X.G.; Wang, J.; Chen, W.B.; Feng, X.L.; Wang, D.; Song, C.Y.; Zeng, S.Q. Elemental geochemistry of the early Jurassic black shales in the Qiangtang Basin, eastern Tethys: Constraints for palaeoenvironment conditions. *Geol. J.* **2016**, *51*, 443–454. [CrossRef]
69. McLennan, S.M. Rare earth elements in sedimentary rocks: Influence of provenance and sedimentary processes. *Rev. Mineral. Geochem.* **1989**, *21*, 169–200.
70. Taylor, S.R.; McLennan, S.M. The Continental Crust: Its Composition and Evolution. *J. Geol.* **1985**, *94*, 57–72.
71. Boynton, W.V. Geochemistry of the rare earth elements: Meteorite studies. In *Developments in Geochemistry*; Henderson, P., Ed.; Elsevier: Amsterdam, The Netherlands, 1984; pp. 63–114.
72. Lu, J.; Vecchi, G.A.; Reichler, T. Expansion of Hadley cell under global warming. *Geophys. Res. Lett.* **2007**, *34*, L06805.
73. Johanson, C.M.; Fu, Q. Hadley cell widening: Model simulations versus observation. *J. Clim.* **2009**, *22*, 2713–2725. [CrossRef]
74. Hasegawa, H.; Tada, R.; Jiang, X.; Suganuma, Y.; Imsamut, S.; Charusiri, P.; Ichinnorov, N.; Khand, Y. Drastic shrinking of the Hadley circulation during the mid-Cretaceous Supergreenhouse. *Clim. Past* **2012**, *8*, 1323–1337. [CrossRef]
75. Samanta, A.; Bera, M.K.; Ghosh, R.; Bera, S.; Filley, T.; Pande, K.; Rathore, S.S.; Rai, J.; Sarkar, A. Do the large carbon isotopic excursions in terrestrial organic matter across Paleocene-Eocene boundary in India indicate intensification of tropical precipitation? *Palaeogeogr. Palaeoclimatol. Palaeoecol.* **2013**, *387*, 91–103. [CrossRef]
76. Abels, H.A.; Lauretano, V.; Yperen, A.V.; Hopman, T.; Zachos, J.C.; Lourens, L.J.; Gingerich, P.D.; Bowen, G.J. Carbon isotope excursions in paleosol carbonate marking five early Eocene hyperthermals in the Bighorn Basin, Wyoming. *Clim. Past* **2015**, *11*, 1857–1885.
77. Ferrier, K.L.; Kirchner, J.W.; Finkel, R.C. Weak influences of climate and mineral supply rates on chemical erosion rates: Measurements along two altitudinal transects in the Idaho Batholith. *J. Geophys. Res.* **2012**, *117*, F02026. [CrossRef]
78. Bluth, G.S.; Kump, L.R. Lithologic and climatic controls of river chemistry. *Geochim. Cosmochim. Acta* **1994**, *58*, 2341–2359. [CrossRef]
79. Millot, R.; Gaillardet, J.; Dupre, B.; Allegre, C.J. The global control of silicate weathering rates and the coupling with physical erosion: New insights from rivers of the Canadian Shield. *Earth Planet. Sci. Lett.* **2002**, *196*, 83–98. [CrossRef]
80. Rasmussen, C.; Brantley, S.; Richter, D.B.; Blum, A.; Dixon, J.; White, A.F. Strong climate and tectonic control on plagioclase weathering in granitic terrain. *Earth Planet. Sci. Lett.* **2011**, *301*, 521–530. [CrossRef]
81. Perri, F. Chemical weathering of crystalline rocks in contrasting climatic conditions using geochemical proxies: An review. *Palaeogeogr. Palaeoclimatol. Palaeoecol.* **2020**, *556*, 109873. [CrossRef]
82. Sheldon, N.D.; Retallack, G.J.; Tanaka, S. Geochemical climofunctions from North American Soils and Application to Paleosols across the Eocene-Oligocene Boundary in Oregon. *J. Geol.* **2002**, *110*, 687–696. [CrossRef]
83. Korasidis, V.A.; Wing, S.L.; Nelson, D.M.; Baczynski, A.A. Reworked pollen reduces apparent floral change during the Paleocene-Eocene Thermal Maximum. *Geology* **2022**, *50*, 1398–1402. [CrossRef]
84. Zhang, S.B.; Gao, Q.Q.; Liu, C.; Jin, Z.X.; Lu, L.Z. Paleomagnetic characteristics of eogene system and its basal boundary on northwest margin of Jianghan Basin. *Acta Pet. Sin.* **1992**, *13*, 121–126.

85. Kiehl, J.T.; Shields, C.A.; Snyder, M.A.; Zachos, J.C.; Rothstein, M. Greenhouse- and orbital-forced climate extremes during the early Eocene. *Phil. Trans. R Soc. A* **2018**, *376*, 20170085. [CrossRef] [PubMed]
86. Wang, Y.X.; Xu, S.; Hao, F.; Poulton, S.W.; Zhang, Y.Y.; Guo, T.X.; Lu, Y.B.; Bai, N. Arid climate disturbance and the development of salinized lacustrine oil shale in the Middle Jurassic Dameigou Formation, Qaidam Basin, northwestern China. *Palaeogeogr. Palaeoclimatol. Palaeoecol.* **2021**, *577*, 110533. [CrossRef]
87. Meybeck, M.; Laroche, L.; Dürr, H.H.; Syvitski, J.P.M. Global variability of daily total suspended solids and their fluxes in rivers. *Glob. Planet. Change* **2003**, *39*, 65–93. [CrossRef]
88. Alexandrov, Y.; Cohen, H.; Laronne, J.B.; Reid, I. Suspended sediment load, bed load, and dissolved load yields from a semiarid drainage basin: A 15-year study. *Water Resour. Res.* **2009**, *45*, W08408. [CrossRef]
89. Duvert, C.; Gratiot, N.; Evrard, O.; Navratil, O.; Némery, J.; Prat, C.; Esteves, M. Drivers of erosion and suspended sediment transport in three headwater catchments of the Mexican Central Highlands. *Geomorphology* **2010**, *123*, 243–256. [CrossRef]
90. Gallart, F.; Pérez-Gallego, N.; Latron, J.; Catari, G.; Martínez-Carreras, N.; Nord, N. Short- and long- term studies of sediment dynamics in a small humid mountain Mediterranean basin with badlands. *Geomorphology* **2013**, *196*, 242–251. [CrossRef]
91. Grove, M.K.; Bilotta, G.S.; Woockman, R.R.; Schwartz, J.S. Suspended sediment regimes in contrasting reference-condition freshwater ecosystems: Implications for water quality guidelines and management. *Sci. Total Environ.* **2015**, *502*, 481–492. [CrossRef]
92. Rodríguez-Blanco, M.L.; Taboada-Castro, M.M.; Taboada-Castro, M.T. An overview of patterns and dynamics of suspended sediment transport in an agroforest headwater system in humid climate: Results from a long-term monitoring. *Sci. Total Environ.* **2019**, *648*, 33–43. [CrossRef] [PubMed]